Experimental observation of the surface anomalous Hall effect in $CoNi_3$ (001) epitaxial films

Xinru He,[1,*] Lei Wang,[2,*] Ke Xia,[2,†] and S. M. Zhou[1,3,‡]

[1]*Shanghai Key Laboratory of Special Artificial Microstructure Materials and Technology and Pohl Institute of Solid State Physics and School of Physics Science and Engineering, Tongji University, Shanghai 200092, China*

[2]*School of Physics, Southeast University, Nanjing 211189, China*

[3]*School of Materials Science and Engineering, Anhui University, Hefei 230601, China*

(Received 15 November 2023; revised 29 February 2024; accepted 1 March 2024; published 20 March 2024)

Along with the progression of the low-dimensional materials, the high-quality thin film and two-dimensional material come into the stage of spintronics, where the surfaces should be important or even dominate the transport phenomena. For anomalous Hall effect (AHE), however, the surfaces are mainly treated as an additional scattering source to the residual resistance, and the corresponding AHE is submerged by the bulk contributions. In this work, we have disentangled contributions from the surface and the bulk to the AHE in $CoNi_3$ (001) epitaxial and $CoNi_3$ polycrystalline films by varying thickness and temperature. The surface and the bulk anomalous Hall angles are found to have opposite signs for all temperatures and the corresponding surface anomalous Hall angles are surprisingly much larger than the bulk anomalous Hall angles. Furthermore, the first-principles calculations are carried out and the observed surface AHE is successfully replicated.

DOI: 10.1103/PhysRevB.109.104422

I. INTRODUCTION

Since the first discovery of anomalous Hall effect (AHE) in ferromagnetic metals in 1881 [1], extensive research has been conducted both theoretically [2–6] and experimentally [7–13] to uncover its intriguing mechanism. One may also notice that the corresponding research objects are mainly considered as bulk materials while neglecting the surface effect, as the conducting electrons intuitively travel inside the material for a thick film.

However, as reported for the spin Hall effect (SHE), differences of orders of magnitude had been found when measuring the spin Hall angle in the same materials by different groups [14,15]. This incongruity had been solved by proposing an interface SHE [16], which contributes a finite effective spin Hall angle even for a film with infinity thickness. Considering that the AHE shares the same physical origin with SHE, it is natural to predict a giant surface/interface AHE, accordingly. However, due to the coherence between the complicated contributions of AHE, the constant surface/interface effect will be submerged by other contributions, e.g., the constant Berry curvature and side jump. Therefore, the surface/interface AHE has kept underneath for a long time.

Furthermore, it is noted that the sheet resistivity consists of the surface and bulk ones, according to the Fuchs-Sondheimer theory [17–19]. Also due to the symmetry breaking on the surface of the film, the surface contributions to the AHE may be different from the bulk one and the anomalous Hall conductivity or resistivity may also depend on the film thickness [20]. Up to date, the surface/interface contribution to the AHE has been neglected in most of such studies.

On top of the above considerations, in this work, we studied the surface contribution to the AHE in $CoNi_3$ (001) epitaxial and polycrystalline films, fabricated by magnetron sputtering, due to the intrinsic contribution of AHE in $CoNi_3$(001) alloy is very small [12], and thereby it is favorable to separate the interface scattering from the bulk ones. Our results show that θ_{AH} changes from negative to positive and approaches a constant as the film thickness increases. Therefore, the surface contribution to the anomalous Hall angle (AHA) has an opposite sign to that of the bulk one, which can be reproduced by first-principles calculations. Moreover, the scaling law of the *bulk* $CoNi_3$ is investigated.

II. SAMPLE FABRICATION AND MEASUREMENTS

A series of high-quality $CoNi_3$ (001) epitaxial films with different thicknesses were fabricated on (001) $SrTiO_3$ (STO, space group $Pm\overline{3}m$, lattice constant $a = 0.3905$ nm) by direct current (dc) magnetron sputtering, respectively. Alloy targets with specific atomic percentages (Co:Ni=1:3) were used for deposition. The base pressure was better than 3×10^{-6} Pa and the working Ar pressure was 0.3 Pa. The STO substrates were kept at 150 °C during deposition. After deposition, the samples were elevated to 500 °C for 2 hours to obtain a high-quality single-crystalline structure. The deposition rate of $CoNi_3$ films was about 0.18 nm/s. For comparison, $CoNi_3$ polycrystalline films were deposited on Si(111) substrates with native oxide at room temperature. Finally, 2.0 nm thick Al_2O_3 layers were deposited to prevent oxidation. The films thickness and the microstructure were characterized by x-ray reflection (XRR) and x-ray diffraction (XRD), respectively, by using a Bruker D8 diffractometer with

*These authors contributed equally to this work.

†kexia@seu.edu.cn

‡shiming@tongji.edu.cn

 ©2024 American Physical Society

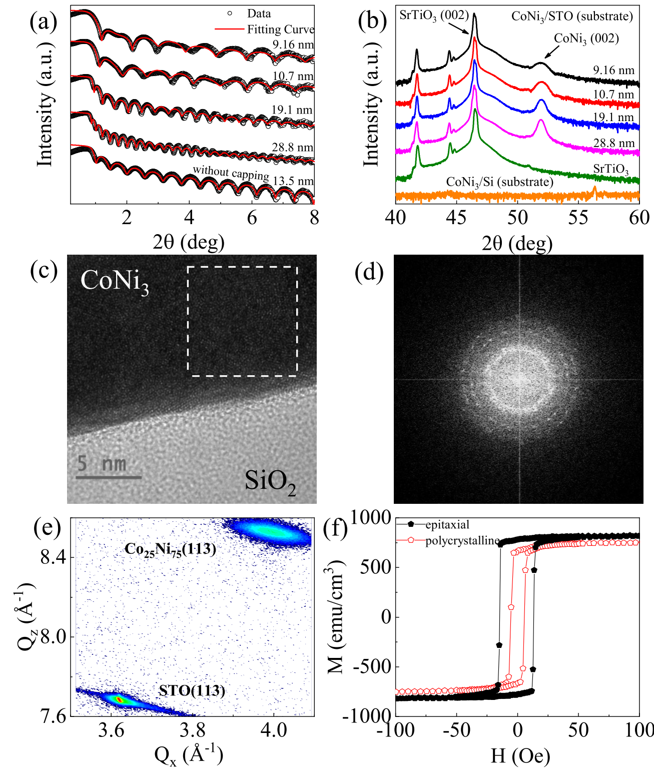

FIG. 1. (a) XRR spectra of epitaxial $CoNi_3$ (001) films on $SrTiO_3$ (001) substrate with 2 nm Al_2O_3 capping layer, including the film with thickness of $t = 13.5$ nm without Al_2O_3 capping layer. (b) XRD spectra of epitaxial $CoNi_3$ (001) films on $SrTiO_3$ (001) substrate and $CoNi_3$ polycrystalline film on natural oxidized Si substrate. (c) HRTEM pattern of polycrystalline $CoNi_3$ (15 nm) film on natural oxidized Si (substrate) and (d) SAED pattern of the region marked by the dashed line of (c). (e) RSM of epitaxial $CoNi_3$ (001) film and (f) magnetization hysteresis loops of $CoNi_3$ (001) epitaxial and polycrystalline films. All the measurements were performed at room temperature. In (a), the results of 13.5 nm thick $CoNi_3$ (001) film without Al_2O_3 capping layer are also given. The open circles refer to measured data and the red lines refer to the fitted results. In (b), the results of polycrystalline $CoNi_3$ (15 nm) on natural oxidized Si (substrate) are also given. In (a),(b), the inset numbers refer to the film thickness. In (f), the external magnetic field is applied along the [110] orientation for $CoNi_3$ (001) epitaxial films. In (e),(f), the film thickness is $t = 50$ nm.

Cu $K_\alpha(\lambda = 0.1542$ nm) and 5-axis configuration. In order to further show the microstructure, high-resolution transmission electron microscopy (HRTEM) and selected area electron diffraction (SEAD) measurements were performed on typical samples. Magnetization hysteresis loops were measured by vibrating sample magnetometer (VSM) at room temperature. Measurements of AHE were performed by physical properties measurement system (PPMS).

III. RESULTS AND DISCUSSION

Figure 1(a) shows the XRR spectra of $CoNi_3$(001) epitaxial films on $SrTiO_3$(STO) substrates with 2 nm Al_2O_3 capping layer, where the film with thickness of $t = 13.5$ nm has no capping layer. The film thickness of $CoNi_3$ is characterized by the interference fringes with different oscillation periods in the XRR spectra. For all samples, the interference fringes can be observed in a wide-angle region from the critical angle $2\theta \approx 1.0^\circ$ to 8.0°. The fitted value of the film thickness is close to the designated one and the roughness of the top surface of $CoNi_3$ for samples with and without Al_2O_3 capping layer is fitted to be about 0.2 nm. Figure 1(b) shows the corresponding XRD patterns of $CoNi_3$ epitaxial films on STO substrates and $CoNi_3$ polycrystalline film on Si/SiO_2 substrate, in which two peaks are found at $2\theta = 46^\circ$ and 52°, which correspond to face-centered cubic (fcc) STO (002) and CoNi (002) orientations, respectively. Meanwhile, the intensity of CoNi (002) peak varies with film thickness, and the grain size is expected to increase when the film becomes thick, according to the Scherrer formula [21]. The orange line in Fig. 1(b) referring to the polycrystalline $CoNi_3$ film has no diffraction peak, indicating that there is no preferred texture. In order to further explore the morphology of the polycrystalline films, the HRTEM and SAED measurements were performed and plotted in the Figs. 1(c) and 1(d). It can be seen that the atomic arrangement does not show any crystal structure. Meanwhile, the SAED pattern shows an obvious diffuse ring and several concentric rings that are not bright enough. The results in Figs. 1(b)–1(d) indicate that the polycrystalline films have no preferred orientation although it is a single phase.

The reciprocal-space mapping (RSM) in Fig. 1(e) well confirms the epitaxial growth of the $CoNi_3$ (001) film. The (113) peak can be decomposed as

$$(113) = 1 \cdot (110)_{ip} + 3 \cdot (001)_{op} \tag{1}$$

In this case, the lattice constants a, b, and c can be calculated from the following relationship [22]

$$a = b = \frac{\sqrt{2}}{Q_x}, \quad c = \frac{3}{Q_z}, \tag{2}$$

where Q_x and Q_z are the position of a reciprocal lattice point in the epitaxial $CoNi_3$ (001) films. The lattice constant can be obtained from the peak positions of STO substrate and $CoNi_3$ film in the mapping plot. The lattice constants of the STO substrate and the $CoNi_3$ film are found to be $a = 0.3908$ nm and 0.3542 nm, $c = 0.3905$ and 0.3517 nm, respectively. Figure 1(f) shows the magnetization hysteresis loops of the epitaxial $CoNi_3$ (001) and polycrystalline $CoNi_3$ films with the film thickness $t = 50$ nm. For epitaxial $CoNi_3$ (001) films, the external magnetic field is applied parallel to [110] in film plane. With the remanent ration $M_r/M_s = 0.97$, the easy axis is parallel to the [110] orientation, in agreement with the negative and small fourfold magnetocrystalline constant K_1 of $CoNi_3$ [23]. The saturation magnetization M_s of the epitaxial and polycrystalline films is about 800 emu/cm^3 and 760 emu/cm^3, respectively, close to the results of the Slater-Pauling curve [24]. The coercivity of epitaxial $CoNi_3$ (001) films, 14.0 Oe, is larger than that of polycrystalline $CoNi_3$ films, 5.5 Oe, due to the averaging of the small magnetocrystalline anisotropy in the polycrystalline films.

The surface anomalous Hall effect can be understood by means of Fig. 2(a). Compared with conventional AHE, it will mutate on the surface of the magnetic film, thus showing

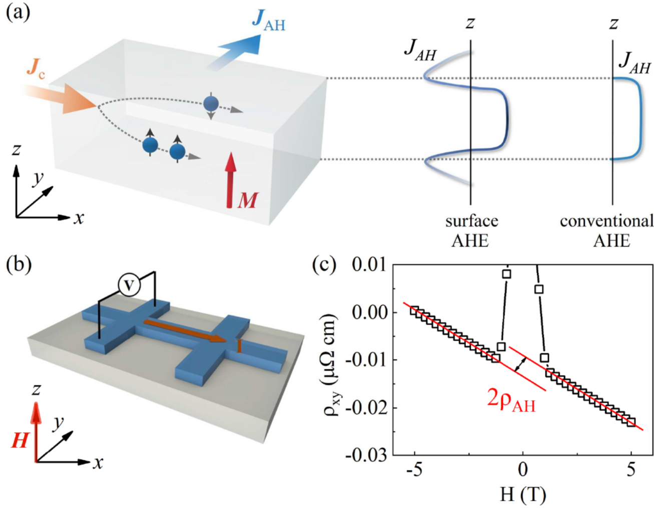

FIG. 2. Schematics of interface AHE (a) and AHE measurement (b). (c) Typical Hall resistivity ρ_{xy} versus out-of-plane H for the $CoNi_3$ epitaxial film with thickness $t = 50$ nm, measured at $T = 300$ K.

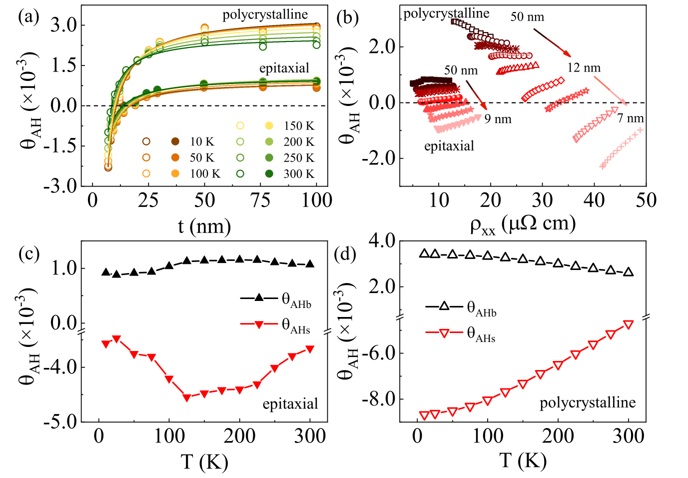

FIG. 3. (a) Thickness dependence of $\theta_{\rm AH}$ for epitaxial (solid symbols) and polycrystalline (open symbols) films at various temperatures, (b) $\theta_{\rm AH}$ versus ρ_{xx} for epitaxial (solid symbols) and polycrystalline (open symbols) films by varying temperature. The solid lines in (a) are fitted results based on Eq. (6). The fitted results of the bulk and surface AHAs, $\theta_{\rm AHb}$ (black squares) and $\theta_{\rm AHs}$ (red circles) in epitaxial (c) and polycrystalline (d) films, as a function of temperature. The inset numbers in (a) and (b) refer to the measurement temperature and the film thickness, respectively.

the thickness dependence that will be described later. Before measurements of the longitudinal resistivity ρ_{xx} and the Hall resistivity ρ_{xy}, flat films were patterned into Hall bar by micronano processing, as shown in Fig. 2(b). The current in the Hall bar is aligned along [100] of $CoNi_3$ (001) epitaxial films. The Hall resistivity ρ_{xy} was measured as a function of the external magnetic field H, where H is perpendicular to the film plane. It can be seen that a typical Hall loop of $t = 50$ nm is shown in Fig. 2(c) and the anomalous Hall resistivity $\rho_{\rm AH} = (\rho_{xy}^{+} - \rho_{xy}^{-})/2$, where ρ_{xy}^{+} and ρ_{xy}^{-} are the extrapolated values of ρ_{xy} from positive and negative high magnetic fields.

Figure 3(a) shows the film thickness dependence of $\theta_{\rm AH}$, defined as the ratio ρ_{AH}/ρ_{xx}, at various temperatures for $CoNi_3$ (001) epitaxial films (solid symbols). For comparison, the results of $CoNi_3$ polycrystalline films (open symbols) are also given. As the films thickness increases, the $\theta_{\rm AH}$ in both epitaxial and polycrystalline films approaches positive constants whereas it approaches negative ones as the film thickness $t \to 0$. Therefore, $\theta_{\rm AH}$ of both epitaxial and polycrystalline films changes its sign with thickness. Moreover, the $\theta_{\rm AH}$ of polycrystalline films is larger than that of epitaxial films due to increased scattering events. Meanwhile, the longitudinal resistivity in the $CoNi_3$ polycrystalline films varies in a much wider range than that of epitaxial ones when T changes from 10 K to 300 K, as shown in Fig. 3(b). Furthermore, several features also occur in Fig. 3(b). Firstly, for thin polycrystalline films, $\theta_{\rm AH}$ increases with increasing ρ_{xx}. The variation trend changes gradually with the film thickness and finally $\theta_{\rm AH}$ decreases with increasing ρ_{xx} for $t > 25$ nm. Secondly, $\theta_{\rm AH}$ is negative for thin films and positive for thick films. Thirdly, the evolution of the curve θ_{AH} versus ρ_{xx} with the film thickness is similar in $CoNi_3$ (001) epitaxial and $CoNi_3$ polycrystalline films.

Moreover, to distinguish different contributions of AHE, we have tried to separate the experimentally measured $\theta_{\rm AH}$ into bulk and surface terms. Within the frame of the mean-free path, the charge-current density distribution along the normal direction of the thin film (z, as shown in Fig. 4) can be expressed as [17,18,25]

$$j_c(z) = \mathcal{A}\mathbf{E} \times \int_0^{\frac{1}{2}\pi} \sin^3\alpha \left\{1 - \exp\left(-\frac{t}{2l\cos\alpha}\right) \times \cosh\left(\frac{t-2z}{2l\cos\alpha}\right)\right\} d\alpha, \tag{3}$$

where $\mathcal{A}$ is the material-dependent parameter, $\mathbf{E}$ is the applied electric field, α is the scattering angle, t is the thickness of the film, and l is the mean-free path.

Assuming that only the AHA at the surfaces ($\theta_{\rm AHs}$ with $z = 0, t$) is different from the bulk AHA ($\theta_{\rm AHb}$), the z-dependent AHA can be written as

$$\theta_{\rm AH}(z) = \theta_{\rm AHs}\delta(z) + \theta_{\rm AHs}\delta(z-t) + \theta_{\rm AHb}. \tag{4}$$

Thus, the average anomalous Hall current in the thin film is

$$\bar{j}_{\rm AH} = \frac{1}{t}\int_0^t \theta_{\rm AH}(z) j_c(z) dz, \tag{5}$$

together with the average charge current $\bar{j}_c = \frac{1}{t}\int_0^t j_c(z)dz$, the measured AHA can be obtained as

$$\theta_{\rm AH} = \frac{\bar{j}_{\rm AH}}{\bar{j}_c} = \theta_{\rm AHb} + \frac{2f(t,l,0)}{\int_0^t f(t,l,z)dz}\theta_{\rm AHs} \tag{6}$$

with

$$f(t,l,z) = \int_0^{\frac{1}{2}\pi} \sin^3\alpha \left\{1 - \exp\left(-\frac{t}{2l\cos\alpha}\right) \times \cosh\left(\frac{t-2z}{2l\cos\alpha}\right)\right\} d\alpha. \tag{7}$$

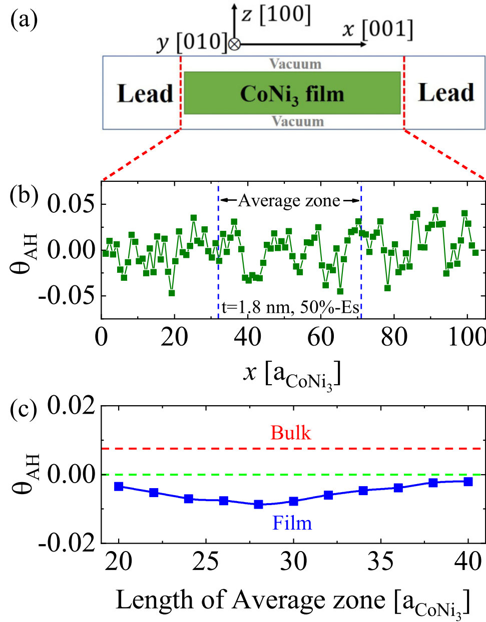

FIG. 4. (a) The sketch of the calculated model of $CoNi_3$ (001) film, where the injecting current is along x axis and the Hall current is perpendicular to the paper (y axis), accordingly. (b) The localized AHA of the $CoNi_3$ (001) film along the transport direction (z), where corresponding thickness is $t \simeq 1.8$ nm and we introduce 50% empty spheres (Es) around the surfaces to describe the roughness of the film. (c) The measured AHA for different lengths of the "average zone" in (b). The red dashed line represents the AHA of bulk $CoNi_3$.

The experimental data in Fig. 3(a) are well fitted by Eqs. (4)–(7), so that the bulk and the surface AHAs are separated as shown in Figs. 3(c)–3(d). Obviously, the surface and bulk AHAs, θ_{AHs} and θ_{AHb}, have opposite signs in the full temperature range. Moreover, the magnitude of θ_{AHs} is larger than that of θ_{AHb} both in epitaxial and polycrystalline films. Furthermore, θ_{AHb} and θ_{AHs} in polycrystalline films are 2–3 times larger than those of epitaxial films, as shown in Figs. 3(c)–3(d), due to large scattering events in polycrystalline films. We also notice that the temperature dependency of θ_{AHs} is stronger than that of θ_{AHb}, which may be attributed to the surface spin wave in the thin film, as the surface spin wave can be more easily excited than the bulk [26,27].

First-principle calculations. The first-principle calculations are carried out to clarify the experimental measurements, as shown in Figs. 4(a)–4(c). Technically, we set up 7×5 supercells of the fcc lattice in the y-z plane with periodic boundary condition and 200 atomic layers of $CoNi_3$ (001) along the x direction between the two leads, as shown in Fig. 4(a). The "vacuum" layers (4 atomic layers in total) are used to disable the corresponding periodic boundary condition along the normal direction to simulate a real film, and 50% empty spheres (Es) are introduced around the surfaces of the film for the surface roughness. For the convergence of the transport calculations, 29×40 $k_{\parallel}$ in y-z plane is used to recover the lateral Brillouin zone, and 10 configurations are used to simulate the random location of Co and Ni atoms in the $CoNi_3$ alloy. All the AHE calculations are carried out by the exact muffin-tin orbitals (EMTOs) based transport code [6,28,29] within the frame of scattering wave functions and the atom-resolved current operators [30–34].

The calculation results of the localized AHA along x direction are plotted in Fig. 4(b), where the AHA θ_{AH} oscillates around zero. Considering that the main part of $CoNi_3$ alloy is Ni, the oscillation should come from the spin spatial precession in Ni [32]. Moreover, the measurements in experiments are on a finite length of the film rather than on a single atomic layer, thus, it should be an average effect inside the "average zone", as shown in Fig. 4(b). Here, to avoid the unexpected influence of the leads, we neglect the data near the leads and only choose the AHA in the middle of the scattering region to obtain the measured AHA as shown in Fig. 4(c). It can be seen that the measured AHA of the film remains negative for various lengths of the average zone. For comparison, the calculated results of the bulk $CoNi_3$ are also plotted in Fig. 4(c) by the red dashed line. Surprisingly, the AHA of bulk $CoNi_3$ is positive. Therefore, this sign difference of the AHA between the bulk and the film strongly demonstrates that the surface contribution of the $CoNi_3$ film is opposite to the bulk contribution, which agree with the experimental results, as discussed above.

The sign change of the AHA in $CoNi_3$ films with film thickness arises from the competition of the surface and the bulk contributions to the AHE. The reason for the difference between bulk and surface AHEs can be attributed to the broken symmetry and potential drop at the surface, where periodic boundary condition along the normal direction of the film vanishes. In this sense, the broken symmetry and potential drop result in the distortion of the band structure and thereby a different intrinsic contribution to the AHE, compared to the bulk. Moreover, there will be additional electron-scattering events on the surface due to both the surface roughness and the barrier of the vacuum. Therefore, both the surface intrinsic contribution and the surface extrinsic contribution (skew scattering and side jump) from scattering events are different from the bulk, accordingly. The present work will also be helpful to understand the experimental results of the AHE in Ni-Fe films, Cr-V-Te single crystals, and $L1_0$ FePt and FePd films [20,35,36], and the surface spin Hall effect [16,37].

The scaling law of AHE. In order to get deep insight into the mechanism of the AHE in epitaxial and polycrystalline $CoNi_3$ films, it is essential to analyze the scaling law of the bulk and surface AHEs. First, the bulk and the surface resistivity are separated from each other. Figures 5(a)–5(b) show the sheet resistivity as a function of the reciprocal film thickness, obeying the Fuchs-Sondheimer model [17–19]. The intercept and the slope correspond to the bulk and the surface resistivity, ρ_{xxb} and ρ_{xxs}, respectively. Apparently, for both epitaxial and polycrystalline films the bulk resistivity changes significantly with temperature whereas the surface resistivity changes little. Meanwhile, the bulk resistivity in polycrystalline films is larger than that of epitaxial films, which is caused by more scattering centers in polycrystalline films compared with those of epitaxial films, as shown in Figs. 3(c)–3(d).

Afterwards, the scaling law of the bulk AHE can be analyzed by varying temperature. According to the definition of θ_{AH}, the anomalous Hall resistivity ρ_{AH} can be expressed as $\rho_{\mathrm{AH}\alpha} = \theta_{\mathrm{AH}\alpha}\rho_{xx\alpha}$, where $\alpha = b, s$ refers to the bulk and

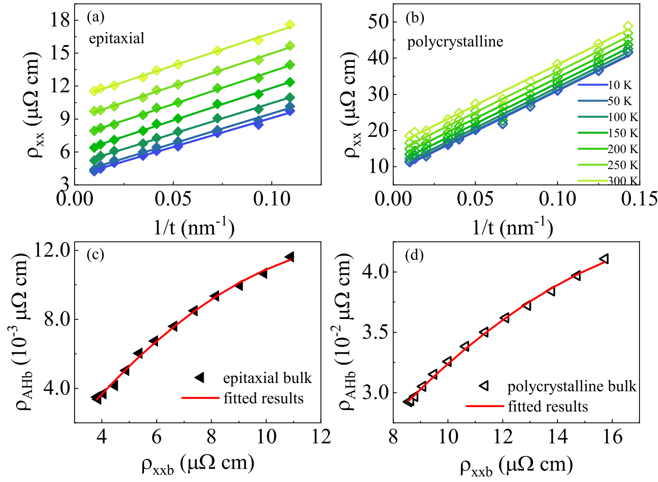

FIG. 5. The sheet resistivity versus the reciprocal film thickness for epitaxial (a) and polycrystalline (b) $CoNi_3$ films at various temperatures. Bulk anomalous Hall resistivity ρ_{AHb} versus bulk resistivity ρ_{xxb} for epitaxial (c) and polycrystalline (d) $CoNi_3$ films. Solid lines in (a), (b), (c), (d) are the fitted results based on Eq. (9) in the main text. The inset numbers in (b) refer to the measurement temperatures in (a), (b).

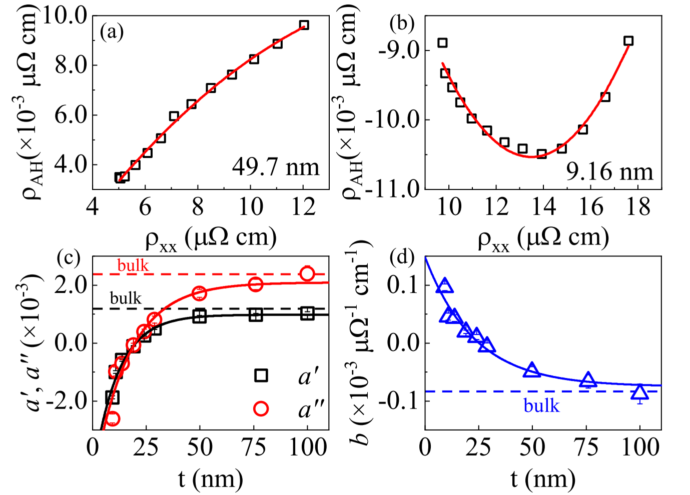

FIG. 6. Measured Hall resistivity ρ_{xy} versus ρ_{xx} for $CoNi_3(001)$ films with $t = 49.7$ nm (a) and 9.16 nm (b), by varying temperature. The solid lines refer to the fitted results based on Eq. (9). Thickness dependencies of the parameters a' and a'' (c), and b (d). The dashed lines in (c) and (d) refer to the fitting results of bulk AHE and the solid lines serve a guide to the eye.

surface AHE, respectively. Figures 5(c) and 5(d) show the bulk anomalous Hall resistivity ρ_{AHb} versus the bulk resistivity ρ_{xxb} to study the scaling law of bulk AHE. Earlier experimental studies showed that the anomalous Hall resistivity obeys the following equation [38,39]:

$$\rho_{AH} = a\rho_{xx} + b\rho_{xx}^2, \tag{8}$$

with the sheet resistivity ρ_{xx} and parameters a and b. In the skew-scattering mechanism, the first term in Eq. (8), the electrons are scattered asymmetrically by the impurity in the presence of the spin orbital coupling [40,41]. As a pure band-structure effect, the intrinsic one in the second term in Eq. (8), first proposed by Karplus and Luttinger [42], can be expressed in terms of the Berry curvature in modern theory [43,44]. The mechanism of the side jump, also included in the second term in Eq. (8), the electrons exhibit coordinate shifts when hitting an impurity [41]. Very recently, a new scaling law has been proposed, in which the contributions to ρ_{AH} from phonons and impurities should not be conflated, and it is rewritten as [7]

$$\rho_{AH} = a'\rho_{xx0} + a''\rho_{xxT} + b\rho_{xx}^2, \tag{9}$$

where ρ_{xx0} is the residual resistivity caused by impurities, and ρ_{xxT} $(= \rho_{xx} - \rho_{xx0})$ is phonon-induced resistivity of bulk and surface, respectively. The parameters a' and a'' correspond to the skew scattering induced by the impurity and phonons, and b corresponds to the scattering independent term. For epitaxial and polycrystalline films, bulk anomalous Hall resistivity ρ_{AHb} can be well fitted by Eq. (9), as shown in Figs. 5(c) and 5(d), respectively. For epitaxial films, the parameters in Eq. (9) are fitted to be $a' = 1.20 \times 10^{-3}$, $a'' = 2.38 \times 10^{-3}$, and $b = -8.4 \times 10^{-5}$ $\mu\Omega^{-1}$ cm^{-1}, respectively. It is interesting to find that the fitted results of the bulk contribution are close to those of thick films.

For the polycrystalline films, the parameters in Eq. (9) are $a' = 4.21 \times 10^{-3}$, $a'' = 3.84 \times 10^{-3}$, and $b = -9.2 \times 10^{-5}$ $\mu\Omega^{-1}$ cm^{-1}, respectively. Of great importance, the values of b in epitaxial and the polycrystalline films are close to each other. This indicates that the parameter b is mainly controlled by the electronic band structure, i.e., the Berry curvature. Since the parameters a' and a'' strongly depend on the microstructural properties, such as the impurity and defect distributions, the values of a' and a'' in polycrystalline films are larger than those of epitaxial films. Moreover, in the second term of Eq. (9), phonon-induced scattering is not negligible.

To further confirm the scaling law of the bulk AHE in $CoNi_3(001)$ epitaxial films, we plot the ρ_{AH} versus ρ_{xx} curves of samples for specific film thickness, by varying sampling temperature. Figures 6(a) and 6(b) show typical results of $t = 49.7$ nm and 9.16 nm, respectively. Apparently, in the sampling temperature region, the monotonicity of the curve and the sign of ρ_{AH} are both different for $t = 49.7$ nm and 9.16 nm. In particular, the measured results can also be fitted by Eq. (9) with $a' = 9.16 \times 10^{-4}$ and -1.88×10^{-3}, $a'' = 1.72 \times 10^{-3}$ and -2.60×10^{-3}, and $b = -4.92 \times 10^{-5}$ $\mu\Omega^{-1}$ cm^{-1} and 9.62×10^{-5} $\mu\Omega^{-1}$ cm^{-1}, for $t = 49.7$ nm and 9.16 nm, respectively. The thickness dependencies of the fitted parameters a', a'', and b are summarized in Figs. 6(c) and 6(d). With increasing film thickness, the magnitudes of a', a'', and b increase and approach constants when $t = 100$ nm. The values of $a' = 1.02 \times 10^{-3}$, $a'' = 2.4 \times 10^{-3}$, and $b = -8.77 \times 10^{-5}$ $\mu\Omega^{-1}$ cm^{-1} are very close to the fitted results of the bulk contribution in Figs. 6(c) and 6(d), because the surface AHE becomes negligible for thick films.

In contrast, the scaling law of the surface AHE, i.e., the dependence of ρ_{AHs} on ρ_{xxs} is too complicated, beyond the scaling law, as shown in Figs. 7(a)–7(d). The functional relationship of ρ_{AHs} on ρ_{xxs} is very complicated and does not conform to Eq. (9), as shown in Figs. 7(b) and 7(d). This is partly because the changes of ρ_{AHs} and ρ_{xxs} are much smaller

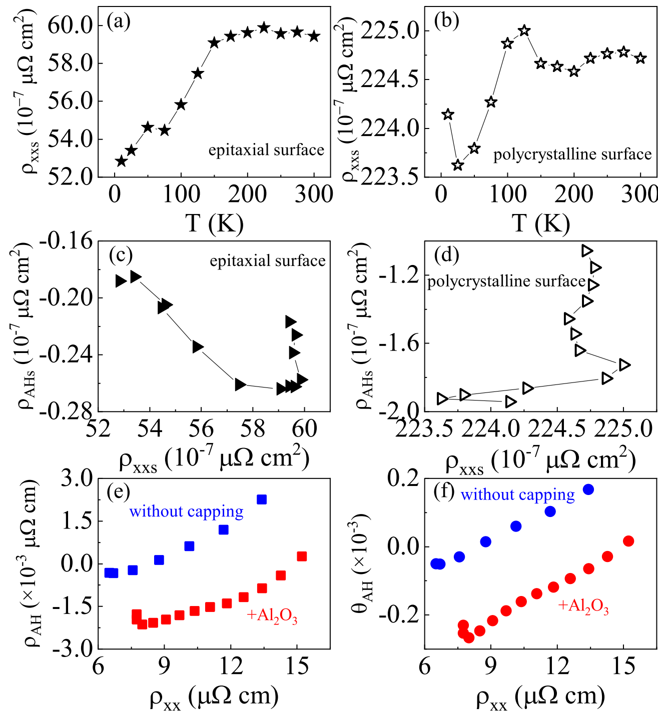

FIG. 7. Temperature dependence of ρ_{xxs} for epitaxial (a) and polycrystalline (b) films, and ρ_{AHs} versus ρ_{xxs} for epitaxial (c) and polycrystalline (d) films. ρ_{AH} (e) and θ_{AH} (f) versus ρ_{xx} of $\mathrm{CoNi_3}$ (001) film with $t = 13.5$ nm, with and without capping layer by varying temperature.

than those of bulk. Moreover, ρ_{xxs} changes nonmonotonically with temperature and tends to a constant as the temperature increases, presenting abnormal performance, as shown in Figs. 7(a) and 7(c). The physical mechanism behind it is very complex. Surface resistivity is caused by surface scattering, including alloy impurities, surface symmetry breaking, and temperature-induced phonon and magnon scattering events. Surface and impurity scattering are generally stronger than the temperature-dependent one. In this way, the contribution of temperature to the surface resistivity is smaller than that of the bulk, so the sensitivity of the surface resistivity to temperature is smaller than that of the bulk. This discrepancy indicates different dimensionality of the surface AHE, compared with that of the bulk one. Considering that the two-center scattering contribution has been demonstrated to be important in AHE [29], the multiple scattering centers in $\mathrm{CoNi_3}$ film, such as the Co/Ni atoms in alloys and the surface/bulk of the film, should produce more complicated scaling law, which will be studied in the future.

Finally, the influence of the capping layer $\mathrm{Al_2O_3}$ on the surface effect was discussed. Experimentally, the results of the $\mathrm{CoNi_3}$ (001) single-layer epitaxial film of $t = 13.5$ nm, without capping layer, was compared with those of the $\mathrm{Al_2O_3/CoNi_3}$ double-layer film, as shown in Figs. 7(e) and 7(f). After adding the capping layer, all data points are shifted downwards and the $\mathrm{Al_2O_3}$ capping layer enhances the surface contributions to the AHE. For samples with $\mathrm{Al_2O_3}$ capping layer, the roughness of the top surface of $\mathrm{CoNi_3}$ (001) films is close to that of films without capping layer and the scattering center on the top surface is expected to be increased, leading to the enhancement of the sheet resistivity and the anomalous Hall resistivity, as shown in Figs. 7(e) and 7(f).

IV. CONCLUSION

Although AHE has been extensively investigated in various ferromagnetic films, the contribution from the surface has rarely been separated. In the present work, we have examined the AHE in $\mathrm{CoNi_3}$ (001) epitaxial and polycrystalline films and distinguished the surface and bulk contributions. At a specific temperature, a sign change of the AHA happens as the film thickness increases. Furthermore, when the sampling temperature increases, the AHA in thick films decreases with the sheet resistivity whereas it increases in thin films. The above phenomena can be attributed to a competition between the surface and bulk effects. In particular, the scaling law of the bulk AHE is revealed. The scattering-independent parameter b is close to each other in epitaxial and polycrystalline films and the side-jump mechanism is negligible. In sharp contrast, since the skew-scattering parameter a' and a'' in polycrystalline films are larger than those of epitaxial films, their magnitudes strongly depend on the electron-scattering events. The experimental results are successfully replicated by first-principles calculations.

ACKNOWLEDGMENTS

This work was supported by the National Key Research and Development Program of China (Grant No. 2022YFA1204002) and National Natural Science Foundation of China (Grant No. 12274323).

[1] E. H. Hall, The London, Edinburgh, and Dublin Philosophical Magazine and Journal of Science **12**, 157 (1881).
[2] S. A. Yang, H. Pan, Y. G. Yao, and Q. Niu, Phys. Rev. B **83**, 125122 (2011).
[3] A. Shitade and N. Nagaosa, J. Phys. Soc. Jpn. **81**, 083704 (2012).
[4] C. Xiao, Y. Liu, M. Xie, S. A. Yang, and Q. Niu, Phys. Rev. B **99**, 245418 (2019).
[5] C. Xiao, H. Zhou, and Q. Niu, Phys. Rev. B **100**, 161403(R) (2019).
[6] L. Wang, T. Min, and K. Xia, Phys. Rev. B **103**, 054204 (2021).
[7] Y. Tian, L. Ye, and X. Jin, Phys. Rev. Lett. **103**, 087206 (2009).
[8] L. Ye, Y. Tian, X. Jin, and D. Xiao, Phys. Rev. B **85**, 220403(R) (2012).
[9] P. He, L. Ma, Z. Shi, G. Y. Guo, J.-G. Zheng, Y. Xin, and S. M. Zhou, Phys. Rev. Lett. **109**, 066402 (2012).
[10] Y. Q. Zhang, N. Y. Sun, R. Shan, J. W. Zhang, S. M. Zhou, Z. Shi, and G. Y. Guo, J. Appl. Phys. **114**, 163714 (2013).
[11] D. Z. Hou, G. Su, Y. Tian, X. F. Jin, S. A. Yang, and Q. Niu, Phys. Rev. Lett. **114**, 217203 (2015).

[12] W. J. Fan, L. Ma, and S. M. Zhou, J. Phys. D **48**, 195004 (2015).
[13] P. J. Wang, P. Chen, Y. Z. Wang, Z. Y. Lian, P. Liu, X. L. Li, Y. Miao, and C. X. Gao, Phys. Rev. B **107**, 094418 (2023).
[14] A. Hoffmann, IEEE Trans. Magn. **49**, 5172 (2013).
[15] J. Sinova, S. O. Valenzuela, J. Wunderlich, C. H. Back, and T. Jungwirth, Rev. Mod. Phys. **87**, 1213 (2015).
[16] L. Wang, R. J. H. Wesselink, Y. Liu, Z. Yuan, K. Xia, and P. J. Kelly, Phys. Rev. Lett. **116**, 196602 (2016).
[17] K. Fuchs, Math. Proc. Camb. Philos. Soc. **34**, 100 (1938).
[18] E. H. Sondheimer, Adv. Phys. **1**, 1 (1952).
[19] D. Schumacher, Thin Solid Films **152**, 499 (1987).
[20] S. J. Xu, Z. Shi, and S. M. Zhou, Phys. Rev. B **98**, 024413 (2018).
[21] P. Scherrer, Nachr. Ges. Wiss. Göttingen, Math.-Phys. Kl. **1918**, 98 (1918).
[22] S. Manzoor, S. Husain, and V. Raghavendra Reddy, Appl. Phys. Lett. **113**, 072901 (2018).
[23] W. J. Fan, L. Ma, Z. Shi, and S. M. Zhou, Chin. Phys. B **24**, 037507 (2015).
[24] S. Chikazum, *Physics of Ferromagnetism* (Clarendon Process, Oxford, 1997).
[25] R. S. Nair and P. J. Kelly, Phys. Rev. B **103**, 195406 (2021).
[26] J. Xiao and G. E. W. Bauer, Phys. Rev. Lett. **108**, 217204 (2012).
[27] C. W. Sandweg, Y. Kajiwara, K. Ando, E. Saitoh, and B. Hillebrands, Appl. Phys. Lett. **97**, 252504 (2010).
[28] L. Wang, K. Shen, S. S. Tsirkin, T. Min, and K. Xia, Appl. Phys. Lett. **120**, 012403 (2022).
[29] L. Wang, T. Min, and K. Xia, Phys. Rev. B **107**, L220402 (2023).
[30] K. Xia, M. Zwierzycki, M. Talanana, P. J. Kelly, and G. E. W. Bauer, Phys. Rev. B **73**, 064420 (2006).
[31] A. A. Starikov, Y. Liu, Z. Yuan, and P. J. Kelly, Phys. Rev. B **97**, 214415 (2018).
[32] S. Wang, Y. Xu, and K. Xia, Phys. Rev. B **77**, 184430 (2008).
[33] R. J. H. Wesselink, K. Gupta, Z. Yuan, and P. J. Kelly, Phys. Rev. B **99**, 144409 (2019).
[34] Z. Chen, Q. Zhang, Y. Zhang, L. Wang, M. Sang, and Y. Ke, Phys. Rev. B **102**, 035405 (2020).
[35] N. Jiang, B. Yang, Y. L. Bai, Y. X. Jiang, and S. F. Zhao, Nanoscale **13**, 11817 (2021).
[36] H. Y. Gu, J. J. Tian, C. Y. Kang, L. S. Wang, R. Pang, M. N. She, K. Liu, L. M. She, Y. H. Song, X. S. Liu, and W. F. Zhang, Appl. Phys. Lett. **121**, 191906 (2022).
[37] Y. Dai, S. J. Xu, S. W. Chen, X. L. Fan, D. Z. Yang, D. S. Xue, D. S. Song, J. Zhu, S. M. Zhou, and X. P. Qiu, Phys. Rev. B **100**, 064404 (2019).
[38] M. C. Chang and Q. Niu, Phys. Rev. B **53**, 7010 (1996).
[39] L. Berger, Phys. Rev. B **2**, 4559 (1970).
[40] J. Smit, Physica **21**, 877 (1955).
[41] J. Smit, Physica **24**, 39 (1958).
[42] R. Karplus and J. M. Luttinger, Phys. Rev. **95**, 1154 (1954).
[43] N. Nagaosa, J. Sinova, S. Onoda, A. H. MacDonald, and N. P. Ong, Rev. Mod. Phys. **82**, 1539 (2010).
[44] D. Xiao, M.-C. Chang, and Q. Niu, Rev. Mod. Phys. **82**, 1959 (2010).